

# Branches of triangulated origami near the flat state

Bryan Gin-ge Chen and Christian D. Santangelo

*Department of Physics, University of Massachusetts Amherst, Amherst, MA 01003*

(Dated: June 5, 2022)

Flat origami structures are characterized by a network of folds and vertices joining unbendable plates. For applications to mechanical design and self-folding structures, it is essential to understand the interplay between the set of folds in the flat origami and the possible 3D folded configurations. When deforming a structure that has been folded one can often linearize the geometric constraints, but the degeneracy of the flat state makes a linear approach impossible there. We derive a theory for the second-order infinitesimal rigidity of an initially flat triangulated origami structure and use it to study the set of nearly-flat configurations. We find that locally, this set consists of a number of distinct “branches” which intersect at the flat state. We find numerical and analytical evidence that suggests that the branches are characterized by choosing each internal vertex to either “pop up” or “pop down”.

## I. INTRODUCTION

The development of responsive materials has paved the way to the fabrication of self-folding structures, based on origami, in which flat sheets of a material can be folded along a discrete network of creases into a targeted three-dimensional configuration [1–8]. The strong constraints on how an origami structure can fold suggests their use as the foundation for mechanical metamaterials [9–14] and deployable structures [15, 16]. Yet, a single origami fold pattern can have many different ways of folding [17–19] and, indeed, manipulating an unfolded origami structure in one’s hands illustrates that many structures have a number of folding pathways that can compete with a desired configuration [2, 8, 10, 20]. Furthermore, experiments on self-folding gel origami do not always fold into the expected, programmed shape [1].

To better understand these issues, it is useful to distinguish two notions of floppiness in an origami structure: (1) the number of degrees of freedom,  $D$ , which scales with the perimeter of a generic origami structure and so tends to be constrained [11, 21, 22], and (2) the number of distinct ways of folding a single structure,  $B$ , from a flat sheet. As we discuss later, the flat state of an origami structure is a singularity where  $B$  branches intersect. Consider the triangulated origami structure in Fig. 1 as an example, which shows some of the allowed configurations that it can adopt as a function of three of the fold angles. In this example,  $D = 1$  so the configuration space is locally curve-like; yet,  $B = 4$ , which can be seen as four distinct one-dimensional branches intersecting at the flat, unfolded configuration in the center.

This paper addresses the following question: how many distinct branches does a generic, triangulated origami crease pattern have, and how can those branches be distinguished? We focus on triangulated origami structures because they are marginally rigid while being maximally flexible [21], and because triangulated origami naturally encodes the kinematics of origami with bendable faces more generally [10]. To answer this question, we first show that the small deformations around any initially flat, triangulated rigid origami structure can be

described by the simultaneous solutions of a system of quadratic equations (Section II). If there are  $V_i$  internal vertices, there are  $V_i$  such equations, and each equation enforces the vanishing of Gaussian curvature at an internal vertex. We use this formalism to review the geometry of nearly-flat  $n$ -fold single-vertex origami structures and give a new proof of the fact that their configuration spaces look like  $(n - 3)$ -dimensional double cones [23], where the two nappes are distinguished by whether the vertex “pops” up or down [8, 19]. Moving on to the case of triangulated origami with multiple vertices, we provide in Section III numerical evidence from a model of random  $D = 1$  origami squares that the number of

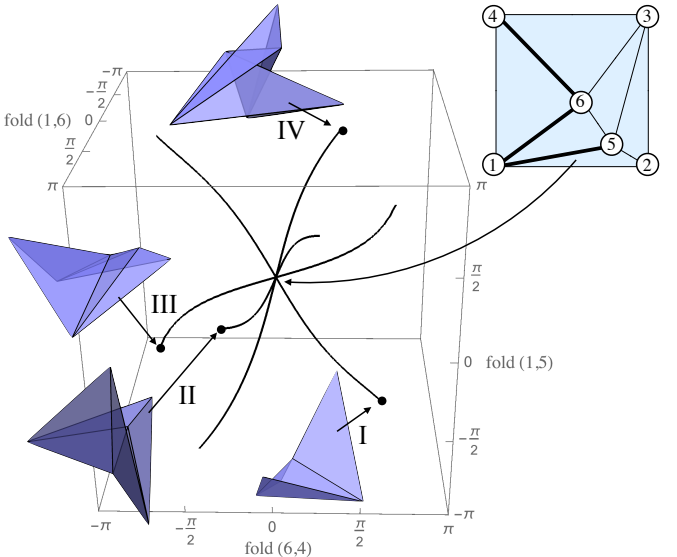


FIG. 1: A neighborhood of the flat state in the configuration space of a two-vertex origami structure (inset) projected onto the fold angles of 3 folds (thick lines). This was computed by solving numerically the length constraint equations. Locally, there are 4 branches, labeled I-IV, each a one-dimensional configuration space, all intersecting at a single point: the flat, unfolded origami state. Supplementary Movies 1-4 show animations of these branches.

branches,  $B$ , is *generically*  $2^{V_i}$  (counted with multiplicity). The branches are not necessarily distinguished by the mountain and valley assignments of the folds, that is, which folds have dihedral angle larger or smaller than  $\pi$  respectively. However, pairs of branches appear to be in one-to-one correspondence with pairs of *vertex sign patterns*, which are assignments of  $\pm 1$  to each internal vertex specifying their popping state. In Section IV we show that a special class of triangulations (roughly, those formed from a sequence of adding degree-3 vertices to the boundary) do satisfy  $B = 2^{V_i}$ . We conclude with a discussion in Section V.

## II. ANALYTICAL METHODS

### A. Model and second-order deformations

Our kinematic model of rigid origami consists of a triangulated network of springs joining vertices in two dimensions which can, upon deformation, come out of the plane (Fig. 2). We will always be considering networks that are planar triangulations of disks (polygons). The edges that are in the interior of the disk will be called *folds*, since we think of the network as a representation of an origami crease pattern. We refer to nonflat configurations of the network as *folded*. Because the network is made from triangles, the angles between adjacent edges will be preserved as long as lengths are preserved. We label the vertices within the origami structure by an integer, and label edges by a pair  $(n, m)$  when the fold joins vertex  $n$  to vertex  $m$ . Using this notation, the kinematic constraints are given by the equations,

$$|\mathbf{X}_n - \mathbf{X}_m|^2 - L_{(n,m)}^2 = 0, \quad (1)$$

for each pair of vertices,  $(n, m)$ , joined by a spring of equilibrium length  $L_{(n,m)}$ . These equations define the *configuration space* of the origami.

We are interested in deformations of flat origami, where the vertices all lie in a single plane. Without loss of generality, we will assume the initial configuration lies in the  $xy$ -plane. We write the position of vertex  $n$  as  $\mathbf{X}_n = \mathbf{U}_n + \mathbf{u}_n + h_n \hat{\mathbf{z}}$ , where  $\mathbf{U}_n$  are the equilibrium positions of the vertex in the  $xy$ -plane,  $\mathbf{u}_n$  is a vertex displacement in the  $xy$ -plane and  $h_n$  is a vertical displacement out of the plane. Expanding Eq. (1) to lowest order in the displacements yields

$$2 \frac{\mathbf{U}_n - \mathbf{U}_m}{|\mathbf{U}_n - \mathbf{U}_m|} \cdot (\mathbf{u}_n - \mathbf{u}_m) + \frac{(h_n - h_m)^2}{|\mathbf{U}_n - \mathbf{U}_m|} \approx 0. \quad (2)$$

Because the vertical displacement decouples from the in-plane displacement and the linear terms in  $h_n$  vanish, any displacement with  $\mathbf{u}_n = 0$  for all  $n$  preserves lengths to first order (i.e. any displacement consisting only of height changes is a first-order flex or motion). But by stopping here we have not captured enough information to see the branches, as the lowest-order information lies in

the quadratic terms of Eq. (2). Since the term quadratic in height leads to a change in bond lengths of the same order as the linear term in the in-plane displacements, we can safely neglect terms of order  $\mathcal{O}(\mathbf{u}_n^2)$ .

The first term of Eq. (2) governs the infinitesimal displacements of the in-plane degrees of freedom. We can rewrite this expression by concatenating the in-plane displacements into a vector  $(\mathbf{u}_1, \mathbf{u}_2, \dots)$ , and define an in-plane compatibility matrix such that row  $(n, m)$  of  $\mathbf{C}$  is defined by the equation

$$\left[ \mathbf{C} \begin{pmatrix} \mathbf{u}_1 \\ \vdots \end{pmatrix} \right]_{(n,m)} = \frac{\mathbf{U}_n - \mathbf{U}_m}{|\mathbf{U}_n - \mathbf{U}_m|} \cdot (\mathbf{u}_n - \mathbf{u}_m). \quad (3)$$

The matrix  $\mathbf{C}$  has pairs of columns indexed by vertices  $n$  and rows indexed by the unique folds  $(n, m)$ . Formally, it maps vectors of in-plane deformations to vectors of in-plane spring displacements and governs the linear deformations of the fold network in the plane.

Since the in-plane deformations and out-of-plane deformations are decoupled in Eq. (2), the in-plane motions are governed (at this order) by the kernel of  $\mathbf{C}$ . And because 2D triangulated networks are generically rigid,  $\ker \mathbf{C}$  is generically generated by translations and rotations. To simplify Eq. 3, we make use of the *self stresses* of  $\mathbf{C}$ , defined by  $\boldsymbol{\sigma}^T \cdot \mathbf{C} = \mathbf{0}^T$ , where  $\boldsymbol{\sigma}$  is a stress vector with components that correspond to each fold and  $T$  is the transpose. Taking the dot product of  $\boldsymbol{\sigma}$  with both sides of Eq. (2), we obtain

$$\sum_{(n,m)} \frac{\sigma_{(n,m)}}{|\mathbf{U}_n - \mathbf{U}_m|} (h_n - h_m)^2 = 0, \quad (4)$$

where  $\sigma_{(n,m)}$  is the component of  $\boldsymbol{\sigma}$  along the fold  $(n, m)$  and the sum is taken over all folds in the network. Thus,

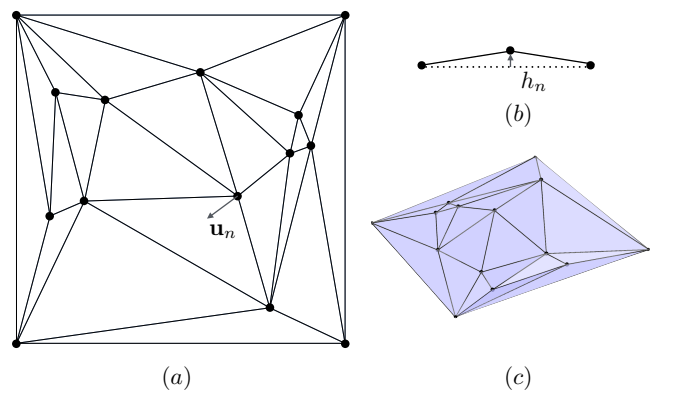


FIG. 2: (a) An origami in the flat state; the vector  $\mathbf{u}_n$  represents the in-plane displacement of vertex  $n$ . (b) A cross-sectional side view near vertex  $n$ ; the scalar  $h_n$  gives the vertical displacement of vertex  $n$ . (c) A small deformation of this origami away from the flat state.

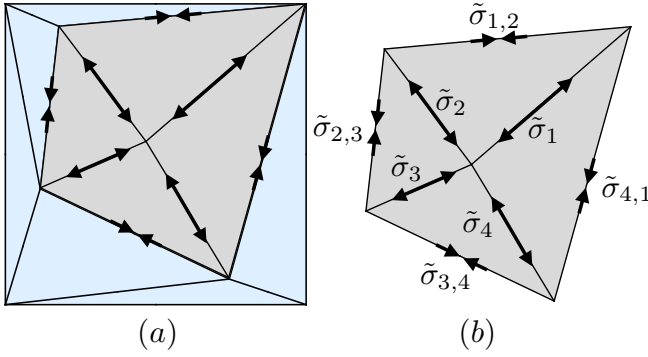


FIG. 3: (a) Extracting a single internal vertex from a larger origami structure. (b) The “wheel stress” for each single vertex, represented as either extensional or compressional arrows, is also present as a self stress in the larger origami structure of (a). Indeed, such wheel stresses form a basis for the space of self stresses of a generic flat triangulated origami, thus the dimensionality of that space is equal to the number of internal vertices. The labels in (b) are associated with Eqs. (6).

each self stress of the in-plane configuration of the fold network gives an equation (4) that constrains the out-of-plane deformations to second order [24].

The solutions to Eq. 4 only give an approximation to the configuration space at the flat state, which may not be a wholly accurate picture, even qualitatively. In all cases that we checked, e.g. in making Fig. (1), second-order approximations did seem to yield true configurations (see Section III). And for single-vertex origami, the second-order motions from the flat state can be shown to extend to actual rigid motions [23, 25], see also Appendix C). However, we know of no such general guarantee, and there are (non-triangulated) origami examples where second-order solutions do not correspond to points lying in the configuration space [25]. Nonetheless, the displacements we will consider can only change the stretching energy to at most sixth-order, so we will mostly ignore this issue in what follows.

## B. Wheel stresses and single-vertex origami

Our first observation is that a flat origami structure with  $V_i$  internal vertices has at least  $V_i$  self stresses. To construct them, we first isolate the faces around each internal vertex and consider the mechanics of the isolated vertex stars apart from the rest of the origami structure (Fig. 3a). Those faces and their edges make a spoked wheel of folds emerging from a single internal vertex and meeting the vertices of a polygon. If there are  $N$  spokes, the  $2N+2$  in-plane positions of the vertices are subject to  $2N$  constraints. Since there are three planar Euclidean motions, there must be generically one self stress (Fig. 3b). This *wheel stress* is preserved if we embed it into the larger structure by setting the remaining components of  $\sigma_{(n,m)}$  to zero.

Interestingly, the constraints arising from the wheel stresses also have a natural geometric interpretation in terms of the Gaussian curvature at each internal vertex, measured by the sum of the angles between adjacent folds around it. We start by generating constraints by enforcing the condition that the Gaussian curvature remains zero at each internal vertex after buckling. To do this, we label the folds around each internal vertex with an index  $I$  which we take modulo the number of folds meeting at the vertex. Then let  $\alpha_{I,I+1}$  be the planar angle between folds  $I, I+1$  and let  $\psi_I$  be the angle the  $I^{th}$  fold makes with respect to the  $xy$ -plane. Spherical trigonometry yields the constraint

$$0 = \sum_I \left\{ \frac{\psi_I \psi_{I+1}}{\sin \alpha_{I,I+1}} - \frac{1}{2} \cot \alpha_{I,I+1} [\psi_I^2 + \psi_{I+1}^2] \right\}, \quad (5)$$

valid up to quadratic order in the  $\psi_I$ . To lowest order, we have  $\psi_{(n,m)} = (h_n - h_m)/|\mathbf{U}_n - \mathbf{U}_m|$  in terms of the height displacements. We thus have an equation for each internal vertex in the form of Eq. (4) from which we can read off a candidate self stress  $\sigma_{(n,m)}$ . If we denote the self stress on the outside edges (on the rim of the wheel) of each vertex by  $\tilde{\sigma}_{I,I+1}$  and the self stress on the spokes  $I$  by  $\tilde{\sigma}_I$  (Fig. 3b), then we obtain

$$\begin{aligned} \tilde{\sigma}_{I,I+1} &= -\csc \alpha_{I,I+1} \frac{\Delta L_{I,I+1}}{L_I L_{I+1}} \\ \tilde{\sigma}_I &= L_{I+1}^{-1} \csc \alpha_{I,I+1} + L_{I-1}^{-1} \csc \alpha_{I-1,I} \\ &\quad - L_I^{-1} (\cot \alpha_{I,I+1} + \cot \alpha_{I-1,I}), \end{aligned} \quad (6)$$

where  $L_I$  is the length of fold  $I$  and  $\Delta L_{I,I+1}^2 = L_I^2 + L_{I+1}^2 - 2L_I L_{I+1} \cos \alpha_{I,I+1}$  (Appendix A). In Appendix B, we prove that Eqs. (6) do give the coefficients of a self stress and thus that the wheel stress constraint is precisely Gaussian curvature preservation.

Let  $Q_{nm}$  be the symmetric matrix corresponding to  $\sigma$  so that the quadratic form in Eq. 4 is written in terms of the vector of vertical displacements at vertices  $\mathbf{h}$ ,

$$\sum_{n,m} Q_{nm} h_n h_m = 0. \quad (7)$$

If the vertex associated with  $Q_{nm}$  has  $N$  folds, we find that the  $(N+1) \times (N+1)$  matrix  $Q_{nm}$  has  $N-2$  nonzero eigenvalues, exactly one of which is negative (Ref. 23 and Appendix C). This is consistent with the notion that a single  $N$ -fold vertex should have  $N-2$  first-order motions once translations and rotations have been removed. Near the flat state, the configuration space of a single vertex is the null-cone of this quadratic form, and since it has one negative eigenvalue, this null-cone has two conical components (*nappes*) that meet at the flat state (Fig. 4a).

Points on the two nappes can be distinguished by the sign of their dot products with the negative eigenvector since the plane normal to the negative eigenvector separates the nappes. This eigenvector gives a set of displacements that maximizes the change in the Gaussian curvature. Indeed, it can be shown from the formulae given

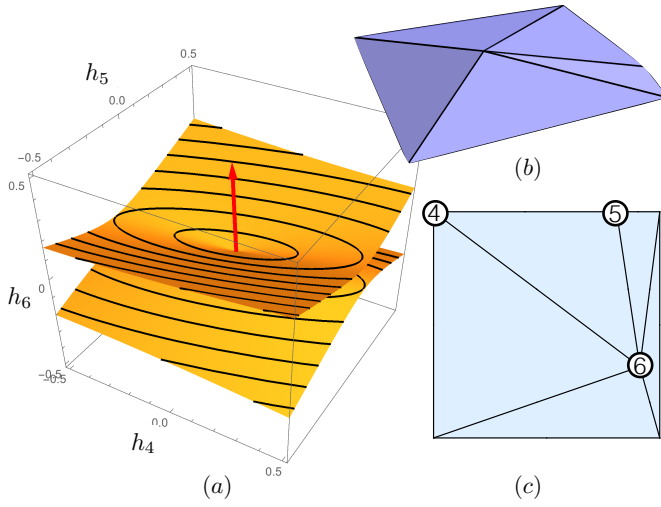


FIG. 4: (a) The configuration space of a five-fold vertex, with three vertices, labeled 1–3, pinned to the  $xy$ –plane for the fold pattern in (c). (b) The eigendeformation of the negative eigenvalue would, on its own, give the vertex positive Gaussian curvature. (c) The planar state with the three labeled vertices, 4–6.

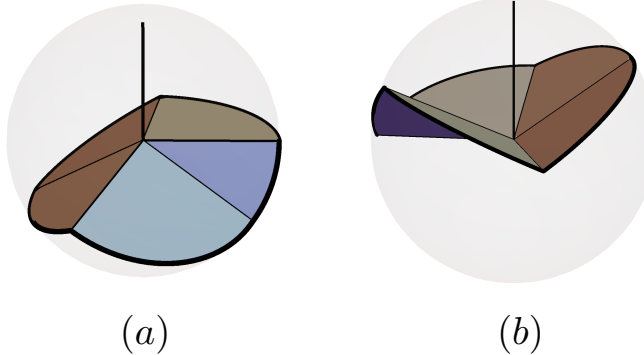


FIG. 5: (a) A 5-fold origami vertex in a popped up configuration; the vertical line depicts the “upwards” normal of the origami surface. (b) The same vertex in a popped down configuration.

in Appendix C that the component of largest magnitude in this eigenvector is the displacement at the vertex itself and the neighboring vertices are moved by smaller amounts in the opposite direction. Such a displacement (Fig. 4b) leads to a conical buckling at the vertex.

These pictures suggest that the difference between rigid origami configurations in the two nappes is related to whether the vertex is buckled up or down (relative to the upwards normal of the origami sheet). We make this more precise in the rest of this subsection.

The *trace* of an origami vertex is defined to be the spherical polygon obtained by intersecting the origami with a small sphere centered at the vertex; it is non-self-intersecting for a vertex sufficiently close to being flat

and thus cuts the sphere into two pieces, corresponding to the upper and lower sides of the origami sheet. Since the trace of a folded origami vertex lies completely in an open hemisphere [26], one of those pieces will have area less than  $2\pi$ . If that piece corresponds to the upper side of the origami, the configuration is called *popped down* and otherwise it is called *popped up* [19] (Fig. 5). Since configurations of these types meet only in the flat state, one of the nappes of the double cone configuration space consists of popped up configurations and the other consists of popped down configurations. Note that Ref. [19] give a simpler definition, where popped down (up) vertices are those whose edge vectors are all in the northern (southern) hemisphere. Our definition is a rotation-invariant generalization that is better suited for considering configurations at vertices that are part of larger multiple-vertex origami.

### C. Consequences for multiple-vertex origami and the definition of branches

Eqs. (4) provide a way to count the number of infinitesimal degrees of freedom of an arbitrary triangulated origami structure, and provide information on the number of distinct ways of folding a given crease pattern from the flat state. Since there are three out-of-plane Euclidean motions, one vertical translation and two rotations about the  $x$ – and  $y$ –axes respectively, we first remove them from consideration by pinning the three vertices of an arbitrary face to the  $xy$ –plane.

Suppose we have an origami crease pattern with  $V_i$  internal vertices and  $V_e$  boundary vertices. Since in-plane displacements are suppressed, there are  $V_i + V_e$  linear degrees of freedom, but  $V_i$  quadratic equations constraining them. We are assuming here that all folds are incident to at least one internal vertex (i.e. we cannot disconnect the origami structure by cutting any one fold). Therefore, the number of degrees of freedom for a flat but otherwise generic triangulation, is given by

$$D = V_e - 3. \quad (8)$$

The term 3 arises from removing the three remaining out-of-plane Euclidean motions. This recovers the count of linear degrees of freedom for a generic (non-flat) triangulated origami [21]. To be more precise, Eq. (8) yields the local dimensionality of the configuration space at nonsingular points.

The flat state, however, is singular as it permits  $D + V_i > D$  linear motions. To better understand the neighborhood of the flat state and, define the notion of “branches” for general  $D$ , we consider the solutions of Eqs. (4), which generally take the form of vectors  $\mathbf{h}$  in  $\mathbb{R}^{V_i+D}$ . Since the quadratic equations are all homogeneous in the vertex heights, any vector  $\lambda \mathbf{h}$  solves Eqs. (4) if  $\mathbf{h}$  does, for any real number  $\lambda$ . Therefore, we are led to consider solutions of Eqs. (4) in *projective space*  $\mathbb{RP}^{V_i+D-1}$ , where a height vector  $h$  is identified with  $\lambda h$

TABLE I: Summary of random triangulation computations

$V_i$	triangulations generated	precision used	systems with $V_t > 0$	MV duplicates
2	100	500	0	0
3	5000	690	0	0
4	1000	690	2	0
5	1000	690	1	17
6	1000	690	1	28
7	300	690	0	17
8	50	690	0	8

for any nonzero real number  $\lambda$ . Finally, we define the *branches* of configuration space to be the connected components of the solutions  $\mathbb{R}\mathbb{P}^{V_i+D-1}$ . Roughly speaking each branch is a connected component of the intersection of a small sphere centered at the flat state with the origami configuration space, modulo the reflection symmetry  $h \mapsto -h$ .

### III. NUMERICAL RESULTS

#### A. Counting branches

We now discuss the case of  $D = 1$  in more concrete terms. In that case, each of the branches corresponds to a curve that passes through the flat state, as in Fig. 1. To understand the typical number of branches  $B$ , we consider a class of random, one-degree-of-freedom origami, generalizing the example of Fig. 1. We generated random origami structures by computing a Delaunay triangulation on the point set consisting of  $V_i$  random points uniformly distributed within a square, together with the corners of the square. We omitted configurations having 3-fold vertices since such vertices are always rigid. We also found no triangulations with edges connecting opposite corners of the square (such edges would break the square into two triangulated triangles, which are also rigid [27]). Since there is a vertex on each corner of the square,  $V_e = 4$  and so  $D = 1$ , no matter how the vertices inside are arranged. We fix the overall position and orientation by setting the height of the vertices of one triangle to zero. To remove the scaling symmetry, we add a normalizing equation  $\sum_j h_j^2 = 1$  to Eqs. (4), resulting in  $V_i + 1$  quadratic polynomials that must be simultaneously solved in terms of  $V_i + 1$  vertex heights, which we do in *Mathematica 11*, which uses a homotopy continuation algorithm for numerical root finding of polynomial systems [28].

We generated several thousand random triangulated origami squares with  $V_i = 2$  to 8 and analyzed their branches (Table I). Accurate solutions seem to require very high precision arithmetic, especially as  $V_i$  becomes larger; to ensure good results we used up to 690 digits of precision and verified the resulting solutions, which allowed us to find solutions up to  $V_i = 8$ .

We numerically computed approximate configurations in our figures by using second-order solutions to perturb the flat configuration and minimizing a stretching energy (sum of squared differences of edge lengths to the lengths in the flat state) on the coordinates until it was zero to high accuracy.

Our main result is that  $B$ , defined to be the number of branches counted with multiplicity, appears to saturate the bound from Bézout's theorem:  $B = 2^{V_i}$ . From the point of view of random quadratic polynomials this is surprising, since one might have expected at least some of the roots to come in complex conjugate pairs. Note that not all crease patterns lead to  $2^{V_i}$  distinct branches. If a crease pattern includes a triangulated triangle, then that triangle is generically rigid up to Euclidean motions (as some evidence, recall that  $D = 0$  when  $V_e = 3$ ; see Ref. [27] for a proof). Triangulated triangles are equivalent to planar projections (Schlegel diagrams) of triangulations of spheres, *e.g.* a degree 3 vertex lies in the center of a projected tetrahedron.

Let  $V_t$  be the number of vertices in the interior of all such triangles. (If we had not excluded crease patterns with degree 3 vertices from our computations, we would count these in  $V_t$ ). These vertices must remain flat in all branches, and it follows that the distinct roots of the quadratic equations must have multiplicity  $2^{V_t}$  from the flat solutions of the  $V_t$  quadratic equations. While triangulated triangles appear to be rare (we found only a handful of  $V_t = 3$  examples that all included a flat octahedron; see Table I), we may account for this effect with the formula

$$B_{\text{distinct}} = 2^{V_i - V_t}. \quad (9)$$

Let us call the  $V_i - V_t$  internal vertices which are not interior to triangulated triangles *foldable vertices*. Note that the heights of non-foldable vertices are determined by the foldable ones by the linear condition that each triangulated triangle is planar, so the configuration space (of  $D$  height displacements) reduces from  $\mathbb{R}^{V_i+1}$  to  $\mathbb{R}^{V_i - V_t + 1}$ .

Following a short Euler characteristic argument, the number of folds (internal edges) for a triangulated square is  $3(V_i - V_t + 1)$ , so the potential number of distinct mountain-valley (MV) assignments is  $2^{3(V_i - V_t + 1)} / 2$  up to a global sign change. Naïvely, the fraction of these MV assignments we can find among the branches is at most  $(1/4)^{V_i - V_t - 1}$ , which approaches zero with increasing number of vertices. However, there are combinatorial consistency constraints on the MV patterns, along the lines of those derived in Ref. [19] for single-vertex origami, so this is certainly an overestimate. We did not attempt to work out these consistency conditions, but as some evidence that they play a role, in our computer-generated examples with  $V_i = 5, 6, 7, 8$  we found an increasing number of fold patterns where multiple branches have coinciding MV assignments (Table I and Section III C). This phenomenon is well-known in the origami community [29] and an illuminating example is the 6-fold origami vertex with alternating mountain and valley folds (MVMVMV

in cyclic order around the vertex) called the “waterbomb structure” [8, 20]. Since the distribution of mountain and valley folds do not distinguish different branches in configuration space, and further, since it is hard to guess which MV assignments are allowed, the question remains, is there anything that does distinguish those branches from each other?

### B. Vertex sign patterns

Given a folded configuration of an origami square with multiple internal vertices, we can ask whether each vertex is popped up or down. These are encoded as *vertex sign patterns*, assignments of  $+1, -1$ , to the foldable vertices if they are popped up, down. (Since the  $V_t$  vertices lying within triangulated triangles are always flat, we could extend the vertex sign pattern to these vertices by assigning them the value 0). As there are therefore  $2^{V_i - V_t}$  choices of vertex sign patterns, it is natural to hope that there is a one-to-one correspondence with the branches. However, we are not distinguishing branches related by the  $z$ -reflection symmetry, so we must identify vertex sign patterns related by a global sign change and we are left with only  $2^{V_i - V_t - 1}$  equivalence classes. Note that in a single 4-fold vertex origami, we have only one vertex sign pattern up to sign and two branches, so instead the best we can hope for is a one-to-one correspondence between *pairs* of branches and sign-related pairs of vertex sign patterns.

We check this correspondence computationally as follows: we first determine the negative eigenvector of  $Q_{nm}$  for each internal vertex  $n$ ,  $\mathbf{e}_n$  (shown as an arrow in Fig. 4). Here we ensure that  $+\mathbf{e}_n$  corresponds to the popping up deformation and we extend the vector with zero components so that its dimension is the same as that of  $\mathbf{h}$ . Then the vertex sign pattern is defined by  $\sigma_n = \text{sgn}[\mathbf{e}_n \cdot \mathbf{h}]$ . Both  $\mathbf{h}$  and  $-\mathbf{h}$  correspond to the same branch, so we associate to each branch a pair of vertex sign patterns related by a global sign change. Remarkably, we find that in *all* of our computed examples, there are exactly two branches with each such pair of sign patterns, in agreement with our guess above!

If we look at the branches as lines intersecting in the singular flat state in the second-order configuration space  $\mathbb{R}^{V_i - V_t + 1}$ , each of the  $\mathbf{e}_n$  defines a hyperplane separating the popped-up configurations at  $n$  from those popped-down there (Fig. 6). The set of all such planes arising from the  $V_i - V_t$  foldable vertices divides  $\mathbb{R}^{V_i - V_t + 1}$  into  $2^{V_i - V_t}$  chambers, each labeled by a different vertex sign pattern. Each of these chambers is topologically the product of an orthant of  $\mathbb{R}^{V_i - V_t}$  with a real line. For instance in Fig. 6, each chamber is topologically a quarter-plane crossed with a line. In these terms, our observation is that the  $2^{V_i - V_t}$  distinct rays of the branches always seem to be distributed so that two rays lie in each of these chambers. Again, from the perspective of random solutions to real quadratic equations, one might have ex-

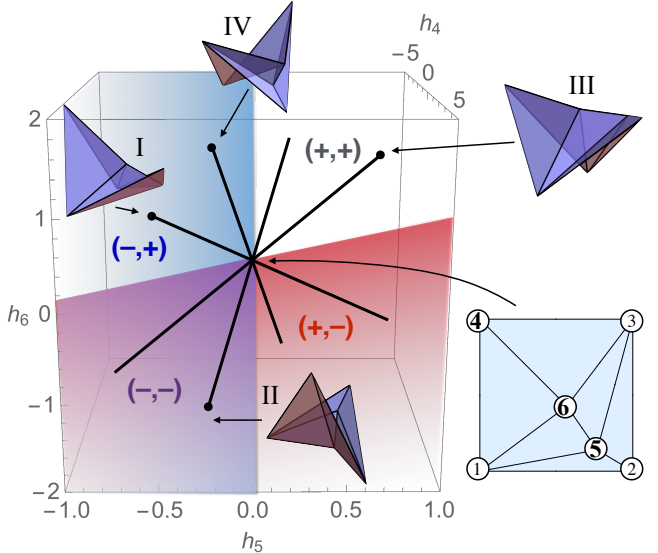


FIG. 6: A view of the configuration space shown in Fig. 1 in height coordinates (only the second-order approximations to the branches are plotted here, so the height units are arbitrary), with the four folded configurations from branches I-IV superimposed. The upper / lower sides of the folded configurations have been colored blue / red, respectively, to make the popping at each vertex more evident. The four vertex sign pattern chambers are defined by the two planes normal to the negative eigenvectors  $\mathbf{e}_5$  and  $\mathbf{e}_6$  (not shown) at the internal vertices 5,6, respectively. The viewpoint is chosen carefully to be “edge-on” to these planes, so that they appear as dividing lines to the four chambers. The patterns are labeled with ordered pairs (sign at vertex 5, sign at vertex 6), so that  $(+,+)$  labels the chamber where vertices 5 and 6 are popped up.

pected some of these branches to be complex conjugate pairs and that the real branches would be distributed much more unevenly in the chambers.

### C. Branches with non-unique Mountain-Valley assignments

We now have two pieces of combinatorial data associated to each branch: first, the well-known assignment of which folds are mountain and which are valleys (MV assignment) and second, the vertex sign pattern (modulo sign). While for most of the origami fold patterns we computed, the branches all have different MV assignments when pairs of branches have identical MV assignments, they can usually be distinguished by the vertex sign patterns, and in particular there is usually exactly one vertex sign that differs. However, as mentioned previously, we did find a number of examples where the two branches with the same vertex sign pattern also have the same MV assignment (Table I).

In Fig. 7 we show a typical origami fold pattern from our data exhibiting two branches with coincident MV assignments. The branches in this example (and most of

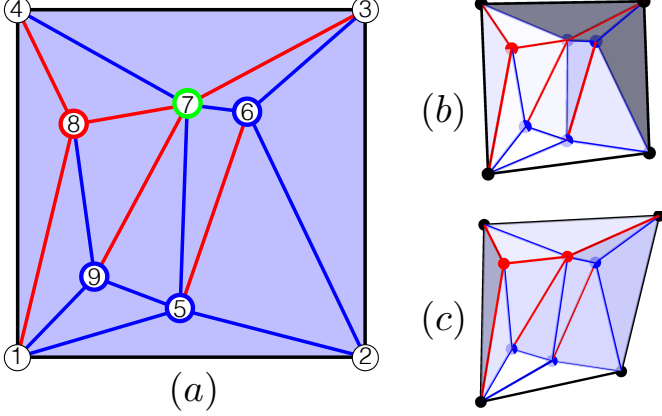


FIG. 7: (a) Crease pattern of a triangulated square with  $V_i = 5$  with a pair of branches where the MV assignments to the edges are identical. Edges colored red and blue represent mountain and valley folds, respectively. Vertices with red and blue outlines represent vertices that are popped up and popped down in both branches, respectively. The state of the green vertex (labeled 7) distinguishes the two branches; i.e. it is popped up in one branch and popped down in the other. (b), (c) give images of folded configurations on the two branches. Supplementary Movies 5-6 show animations of the folding motions along these branches from the flat state.

the other ‘‘MV-coincident pairs’’ we found) can be distinguished by the popping state of exactly one vertex. It follows from Corollary 1 of Ref. [19], that a vertex which can both pop up and pop down must have degree at least 6, and indeed, must contain both a mountain ‘‘bird’s foot’’ and a valley bird’s foot as subsets of the folds around the vertex. Here, a bird’s foot is a sequence of four not-necessarily adjacent folds  $c_1, c_2, c_3, c_4$  in counter-clockwise order around the vertex such that the angles between  $c_1, c_2, c_3$  are between 0 and  $\pi$  and  $c_1, c_2, c_3$  have the same sign (all mountains or all valleys) and  $c_4$  has the opposite sign. Note that the waterbomb vertex contains both a mountain bird’s foot and a valley bird’s foot.

More interestingly, we found a few examples (1 configuration with  $V_i = 5$ , 2 with  $V_i = 6$  and 1 with  $V_i = 7$ , out of the configurations computed for Table I) where MV-coincident branches also had the same vertex sign patterns. The example with  $V_i = 5$  is shown in Fig. 8. In all the examples we computed where branches had coincident MV assignments, they either had exactly one high-degree vertex whose popping state distinguished the branches, or none. We do not dare venture to guess about the relative frequency of such examples as  $V_i$  gets large.

#### IV. H1 TRIANGULATIONS AND BUTTERFLIES

In this section we describe a class of  $D = 1$  triangulations whose configuration spaces are particularly easy to

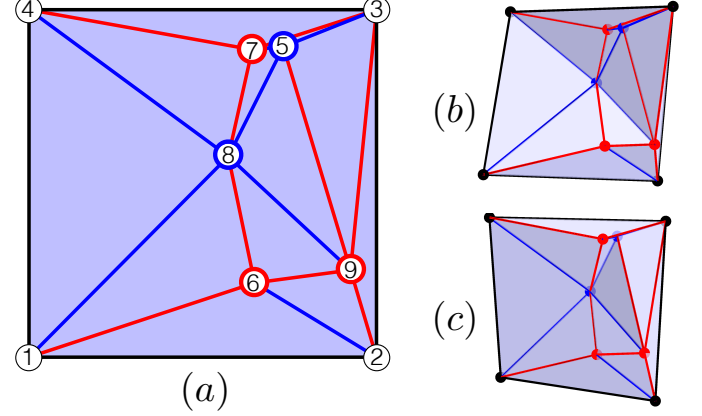


FIG. 8: (a) Crease pattern of a triangulated square with  $V_i = 5$  and a pair of coincident branches, with coloring as in Fig. 7. There is a short fold between vertices 5 and 7 which is a valley fold. In this pair of examples, all vertices are popped the same way in both branches. (b), (c) give images of folded configurations on the two branches. Supplementary Movies 7-8 show animations of the folding motions along these branches from the flat state.

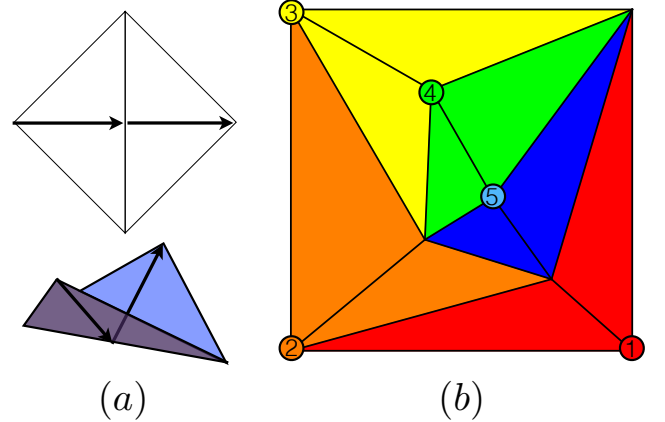


FIG. 9: (color) (a) An illustration of the distance-maximization property of the flat state for a ‘butterfly’. (b) An H1 triangulated origami with  $V_i = 4$ . One possible reduction sequence is depicted, with butterflies and their associated boundary degree-3 vertices colored and labeled in order: (1) red, (2) orange, (3) yellow, (4) green, and ending on (5) the blue seed.

analyze. We will show that near the flat state, their configuration spaces consist of  $2^{V_i}$  intersecting 1D branches. In contrast to most of the rest of our results, we will be discussing actual configurations here, not just second-order approximations.

Henneberg moves [30-32] are rigidity-preserving transformations of graphs that are useful in rigidity theory. We will only consider the Henneberg-1 move, which in three dimensions is just the addition of a degree-3 vertex. In particular, we are interested in triangulations that can be built by repeatedly *adding* degree-3 vertices

to the boundary. To be more precise about the special case we will use, suppose we have some triangulation  $T$ . First choose three vertices  $v_1, v_2, v_3$  on the boundary of  $T$  that are adjacent in the cyclic ordering. Then add a new vertex  $w$  and join it with new edges to  $v_1, v_2, v_3$ . We will say that  $T$  and the resulting triangulation  $T'$  are related by an *H1 move* and will not refer to general Henneberg-1 moves any more. Here we require that  $v_2$  has degree at least 3, as otherwise, it would become a degree 3 vertex in the interior of  $T'$ , and thus be non-foldable.

The key property of H1 moves is that given a configuration of  $T$  where the faces around  $v_2$  are in a non-flat folded configuration, there are always two distinct folded configurations of  $T'$ . To see this, we introduce the notion of butterflies. A *butterfly* is the 1-degree-of-freedom rigid origami consisting of two triangular faces joined by a shared fold (Fig. 9a). Its configuration space is topologically a circle, parametrized by the dihedral angle at the shared fold. Consider the distance  $d$  between the two non-shared vertices of the butterfly. As the dihedral angle varies from 0 to  $2\pi$ , the distance  $d$  decreases monotonically from its maximum value  $d_{max}$  in the planar state, to its minimum value  $d_{min}$  when the butterfly is folded flat, and then increases monotonically again to  $d_f$ . Thus for each value  $d_{min} < d < d_{max}$ , there are two distinct configurations of the butterfly that are related by reflection. Now the claim follows since an H1 move can be viewed as gluing a butterfly at  $v_1, v_2, v_3$ . This is essentially the 3D version of a construction for graphs embedded in the plane described in Ref. [33]. Note that when the faces around  $v_2$  are flat, then  $d$  is maximized and we can only attach the butterfly in its flat state.

The basic idea in the rest of this section will be that triangulations that are reducible by reverse H1 moves to a seed triangulation with a simple configuration space can also be understood easily. Unfortunately, it seems that very few triangulations are reducible at all by a reverse H1 move. We generated 20000 triangulations with  $V_i = 3$  to 8 by the method described in Section III and found that an increasing fraction of triangulations had no degree 3 vertices at the boundary (starting from 0% at  $V_i = 3$  to 88.5% at  $V_i = 8$ ). Furthermore, the number of triangulations in this data set that can be reduced further with more reverse H1 moves appears to decay exponentially.

Nonetheless, we now narrow our focus to triangulations that can be constructed from a sequence of H1 moves from a butterfly (the *seed*). We will call these *H1 triangulations* (Fig. 9b). In line with our observations in the last paragraph, we found that the fraction of H1 triangulations decreased roughly exponentially from 1 at  $V_i = 3$  to 0.0077 at  $V_i = 8$ . (It's not hard to check that under our restriction of no interior degree-3 vertices, all  $V_i = 1, 2, 3$  triangulations are H1).

Note that each reverse H1 move results in the deletion of one boundary vertex and the conversion of one internal vertex to a boundary vertex. This means that a H1 triangulation with  $V_i$  internal vertices can be decomposed

into a sequence of  $V_i$  butterflies. Also, since the seed butterflies always have four boundary vertices, every H1 triangulation also has four boundary vertices. We will assume in this section that the triangulations have no interior degree-3 vertices and also that there are no collinear folds meeting at vertices (there are no “crosses” in the terminology of Ref. [19]), as these nongeneric collinearities can rigidify folds in a flat state.

Let us now discuss the configuration space of H1 triangulations near the flat state. As discussed above, the seed butterfly has a configuration space that is a circle. Now consider the butterfly that is attached by the first H1 move. We showed that there are two distinct ways of attaching it when the seed is nonflat, and one way of attaching it when the seed is flat. We can always choose a small enough interval around the flat state in the configuration space of the seed where the dihedral angle of the new butterfly never reaches  $\pi$ . This implies that a neighborhood of the flat state of the configuration space of the two butterflies together consists of two intersecting lines, topologically a letter X, since we have two choices over every nonzero initial dihedral angle, glued together at the flat state. Continuing, one sees that for each H1 move, the number of 1D branches doubles, and they all still intersect at the flat state. This results in  $2^{V_i}$  branches, as desired.

We have not been able to show that all vertex sign patterns are realized twice, as this would require some analysis of the configurations of the boundary vertices and when they result in popped up / down states of interior vertices after an H1 move. However, one can generalize the arguments in this section to H1-like triangulations where the seed is not just a butterfly but some other simple triangulation, e.g. a single-vertex origami. We hope to elaborate on this elsewhere.

## V. DISCUSSION

Our results have broad importance in using origami techniques to manufacture shapes from flat substrates. In the standard paradigm for self-folding origami, an initially flat sheet is “programmed” by setting the equilibrium dihedral angle of each fold to a nonzero value [2, 8, 10, 20]. Based on the branched structure of configuration space we have found (as exemplified by Fig. 1), once an origami structure begins folding along the wrong branch, it is potentially very difficult to return it to the desired branch. Thus, Ref. [8] introduced the notion that the equilibrium angles should drive the pattern perpendicular to the potential misfolded states.

In order for this to be successful, the branches should be “far apart” by some measure in this space. For instance, one might hope that the branch directions could all be made orthogonal in the  $(3V_i + 1)$ -dimensional space of dihedral angles. While this cannot be true exactly due to the exponential number of branches, it is an interesting open question whether this might be true approxi-

mately, *i.e.* whether, for sufficiently large origami crease patterns, we might have most branches within 99% of being orthogonal, as this happens for random point sets in high dimensions [34]. Some preliminary results have been collected in Appendix D which show that branches tend to be less orthogonal than a uniformly random distribution. It remains to be seen how this impacts the programmability of self-folding origami structures.

We also note that our methods can be applied even to non-triangulated origami. In that case, we would first triangulate the origami, then add additional quadratic constraints to rigidify certain folds. The dimension of the configuration space becomes  $D = V_e - 4 - E$ , where  $E$  is the number of folds in the triangulation that are not in the original pattern. In a recent paper, Stern et al [35] studied examples where  $D = 0$  and they studied branches defined to be minimal-energy directions (as opposed to zero-energy, as in this work) away from the flat state. Intriguingly, the scaling of their  $B$  is exponential in  $\sqrt{V_i}$ . It would be very interesting to understand the crossover between the regime studied in that work and this one.

Proving that each sign-related pair of vertex sign patterns corresponds to a unique pair of folding branches remains elusive. Our problem of finding all branches fits into the broader context of enumeration problems in geometric rigidity such as finding all realizations of isostatic graphs in the plane [33, 36] and enumerating all rigid clusters of sticky hard spheres [37]. The vertex sign patterns seem to impose some structure on the branches in configuration space that leads to the much more tractable formula  $B = 2^{V_i}$  than e.g. the recent recursion formula for the number of complex realizations of isostatic graphs in the plane [36].

Understanding the vertex sign patterns better may be useful for developing robust self-folding structures. In particular it would be interesting to see whether a self-folding paradigm based not only on preferred dihedral angles but also on vertex popping states could be easier to control experimentally, e.g. with conical indenters above and below the sheet. Finally, since MV assignments can be ambiguous, particularly for origami with many internal vertices, perhaps origami crease patterns should be given with vertex sign patterns as well.

### Acknowledgments

We thank the kind hospitality of the Kavli Institute of Theoretical Physics in Santa Barbara, CA and thank Tom Hull and Louis Theran for helpful discussions. This research was supported in part by the National Science Foundation under Grant No. NSF PHY-1125915, and also Grant No. EFRI ODISSEI-1240441.

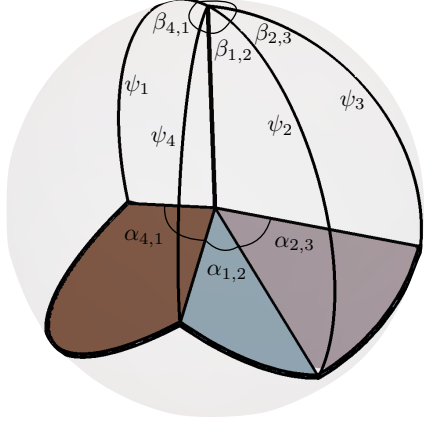


FIG. 10: The spherical polygon spanned by a single vertex. The angle between a fold and the  $\hat{\mathbf{z}}$  axis is  $\psi_i$ , the planar angle between adjacent folds in the plane is  $\alpha_{i,i+1}$  while the angle between adjacent folds at the north pole is  $\beta_{i,i+1}$ . Note that  $\sum_i \beta_{i,i+1} = 2\pi$ .

### Appendix A: Deriving a quadratic constraint for each internal vertex from the vanishing of the Gaussian curvature

One way to express the Gaussian curvature constraint around a single vertex is in terms of the interior angles of the spherical triangle made by a pair of adjacent folds and the  $\hat{\mathbf{z}}$  axis (Fig. 10). We denote  $\alpha_{i,i+1}$  as the planar angle between adjacent folds, which becomes the length of one side of the triangle. Similarly, we denote  $\psi_i$  as the angle between  $\hat{\mathbf{z}}$  and the  $i^{\text{th}}$  fold. Let  $h_0$  be the height of the central vertex, and  $h_i$  be the heights of the vertices around the interior vertex at  $h_0$  and  $L_i$  are the lengths of the folds from  $h_0$  to  $h_i$ . We assume that all quantities are periodic in the index and numbered in counterclockwise order. Then we have angles,

$$\psi_i = \frac{\pi}{2} - \frac{h_i - h_0}{L_i}. \quad (\text{A1})$$

Finally, define the interior angle of the spherical triangle between  $\hat{\mathbf{z}}$  and the two folds as  $\beta_{i,i+1}$  (Fig. 10). The relationship between these angles is given by the spherical law of cosines,

$$\cos \alpha_{i,i+1} = \cos \psi_i \cos \psi_{i+1} + \sin \psi_i \sin \psi_{i+1} \cos \beta_{i,i+1}. \quad (\text{A2})$$

Since the vertices we consider are nearly flat, we will expand around an unfolded configuration in which  $\psi_i = \pi/2$  and  $\beta_{i,i+1} = \alpha_{i,i+1}$ . Therefore, if  $\psi_i = \pi/2 + \delta\psi_i$ ,  $\beta_{i,i+1} = \alpha_{i,i+1} + \delta\beta_{i,i+1}$ , expanding to quadratic order yields

$$\delta\beta_{i,i+1} = \frac{2\delta\psi_i \delta\psi_{i+1} - \delta\psi_i^2 \cos \alpha_{i,i+1} - \delta\psi_{i+1}^2 \cos \alpha_{i,i+1}}{2 \sin \alpha_{i,i+1}}. \quad (\text{A3})$$

The sum of the interior angles  $\sum_i \alpha_{i,i+1} = 2\pi - K$ , where  $K$  is the deficit angle, equivalent to the discrete Gaussian curvature of the vertex; however,  $\sum_i \beta_{i,i+1} = 2\pi$  no matter  $K$ . Therefore, for small  $K$ , we require that

$$\sum_i \delta\beta_{i,i+1} = K. \quad (\text{A4})$$

When the origami is flat,  $K = 0$  at each vertex.

Now we can rewrite the angle  $\delta\beta_{i,i+1}$  in terms of the heights as

$$\begin{aligned} \delta\beta_{i,i+1} = & -\csc \alpha_{i,i+1} \frac{\Delta L_{i,i+1}}{L_i L_{i+1}} \frac{(h_i - h_{i+1})^2}{2\Delta L_{i,i+1}} \\ & + \left( \frac{\csc \alpha_{i,i+1}}{L_{i+1}} - \frac{\cot \alpha_{i,i+1}}{L_i} \right) \frac{(h_i - h_0)^2}{2L_i} \quad (\text{A5}) \\ & + \left( \frac{\csc \alpha_{i,i+1}}{L_i} - \frac{\cot \alpha_{i,i+1}}{L_{i+1}} \right) \frac{(h_{i+1} - h_0)^2}{2L_{i+1}}, \end{aligned}$$

where  $\Delta L_{i,i+1} = \sqrt{L_i^2 + L_{i+1}^2 - 2L_i L_{i+1} \cos \alpha_{i,i+1}}$  is the distance between the vertices at  $h_i$  and  $h_{i+1}$ .

Finally, we have

$$\begin{aligned} 0 = & \sum_i -\csc \alpha_{i,i+1} \frac{\Delta L_{i,i+1}}{L_i L_{i+1}} \frac{(h_i - h_{i+1})^2}{2\Delta L_{i,i+1}} \\ & + \left( \frac{\csc \alpha_{i,i+1}}{L_{i+1}} + \frac{\csc \alpha_{i-1,i}}{L_{i-1}} \right. \\ & \left. - \frac{\cot \alpha_{i,i+1}}{L_i} - \frac{\cot \alpha_{i-1,i}}{L_i} \right) \frac{(h_i - h_0)^2}{2L_i} \quad (\text{A6}) \end{aligned}$$

This is precisely the form of the quadratic constraint that we get from the self stresses in Eq. (4). In the next appendix, we verify that the coefficients here do correspond to a self stress.

## Appendix B: Verification that the Gaussian curvature constraint yields a self stress

Using Eq. (A6), we can immediately read off the components of the stress that would give the quadratic constraint in Eq. (A6). In particular, the stress in the edges along the “rim” of the wheel should be

$$\sigma_{i,i+1} = -\csc \alpha_{i,i+1} \frac{\Delta L_{i,i+1}}{L_i L_{i+1}} \quad (\text{B1})$$

and on the spoke edges

$$\begin{aligned} \sigma_i = & \frac{\csc \alpha_{i,i+1}}{L_{i+1}} + \frac{\csc \alpha_{i-1,i}}{L_{i-1}} \\ & - \frac{\cot \alpha_{i,i+1}}{L_i} - \frac{\cot \alpha_{i-1,i}}{L_i}. \quad (\text{B2}) \end{aligned}$$

What remains to verify is that these do in fact satisfy the equation  $\sigma^T \cdot \mathbf{C} = \mathbf{0}^T$  defining self stresses. Recall that self stresses are assignments of tensions and compressions to edges that preserve force balance at each vertex. Therefore we must check force balance at the spoke vertices (labeled  $i = 1$  to  $N$ ) and the hub vertex 0.

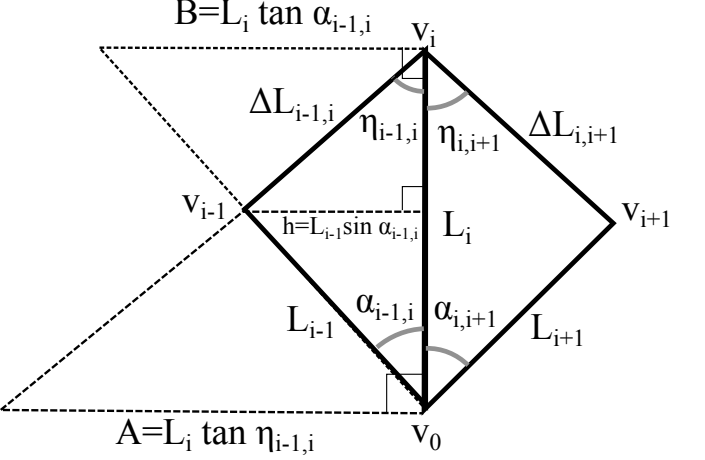


FIG. 11: Trigonometric diagram for verification of force balance at spoke vertex  $i$  along the direction parallel to the spoke. The “crossed ladder” identity relates the lengths of the three parallel dashed lines,  $1/A + 1/B = 1/h$ .

### 1. Force balance at the spokes

We first show force balance at spoke vertex  $i$ . Recall that the position of vertex  $j$  is the vector  $\mathbf{U}_j$  so that  $L_i = |\mathbf{U}_i - \mathbf{U}_0|$  and  $\Delta L_{i,i+1} = |\mathbf{U}_{i+1} - \mathbf{U}_i|$  (Fig. 11). Let’s first check the forces in the direction perpendicular to the spoke edge vector  $(\mathbf{U}_i - \mathbf{U}_0)$ . We only need to use the stresses along the outer edges (Eq. (B1)) for this.

First we use the law of sines on the triangle with sides  $L_i, L_{i+1}, \Delta L_{i,i+1}$  to transform Eq. (B1) to

$$\sigma_{i,i+1} = -\csc \eta_{i,i+1} / L_i, \quad (\text{B3})$$

where  $\eta$  is the angle opposite  $L_{i+1}$ . A similar argument shows that

$$\sigma_{i-1,i} = -\csc \eta_{i-1,i} / L_i, \quad (\text{B4})$$

where  $\eta_{i-1,i}$  is opposite  $L_{i-1}$ .

The magnitudes of the forces perpendicular to the spoke vector are given by  $\sigma_{i,i+1} \sin \eta_{i,i+1} = -\sigma_{i-1,i} \sin \eta_{i-1,i}$  so there is force balance along this direction at vertex  $i$ .

Next we consider the force at vertex  $i$  in the direction parallel to the spoke vector. Using Eqs. (B3) and (B4), we see that the contribution from the two rim edges to the force parallel to the spoke vectors may be written

$$F_{\text{rim},\parallel} = -(\cot \eta_{i-1,i} + \cot \eta_{i,i+1}) / L_i. \quad (\text{B5})$$

$$= F_{\text{rim},\parallel,-} + F_{\text{rim},\parallel,+}$$

$$F_{\text{rim},\parallel,-} = -\cot \eta_{i-1,i} / L_i \quad (\text{B6})$$

$$F_{\text{rim},\parallel,+} = -\cot \eta_{i,i+1} / L_i \quad (\text{B7})$$

Consider the term  $F_{\text{rim},\parallel,-}$ . This is minus the reciprocal of  $L_i \tan \eta_{i-1,i}$  which is the side length  $A$  of a certain right triangle with  $L_i$  as one of its legs (Fig. 11). There is a similar interpretation for the term  $F_{\text{rim},\parallel,+}$ .

Now consider the contribution from the spoke edge given by Eq. (B2). We will split this expression into two pieces, which will each cancel one of the two terms  $F_{\text{rim},\parallel,\mp}$ . The first piece is

$$\csc \alpha_{i-1,i} / L_{i-1} - \cot \alpha_{i-1,i} / L_i. \quad (\text{B8})$$

The first term of Eq. (B8) is the reciprocal of  $L_{i-1} \sin \alpha_{i-1,i}$ , which is the side length  $h$  of a right triangle with  $L_{i-1}$  as the hypotenuse. The second term is the reciprocal of  $L_i \tan \alpha_{i-1,i}$  which is the side length  $B$  of a (different) right triangle with  $L_i$  as one of its legs. See Fig. 11 where these sides are depicted as dashed lines.

The three side lengths  $A, B, h$  are related as in the ‘‘Crossed Ladders problem’’ [38]: for parallel line segments  $A, B, h$  in the configuration shown in Fig. 11, we have the identity  $1/A + 1/B = 1/h$ . Therefore the first part of the force along the spoke edge (Eq. (B8)) cancels  $F_{\text{rim},\parallel,-}$  (Eq. (B6)).

It should be clear that the argument of the preceding three paragraphs can also be carried out for the second piece of Eq. (B2), to show that it cancels  $F_{\text{rim},\parallel,+}$ .

## 2. Force balance at the hub

For force balance at the hub vertex, we proceed with an induction on the number of spokes. For the base case with 3 spokes, we must show that the vectors with lengths  $\sigma_1, \sigma_2, \sigma_3$  directed along the spoke directions sum to zero. Let  $\mathbf{u}_j = (\mathbf{U}_j - \mathbf{U}_0)/|\mathbf{U}_j - \mathbf{U}_0|$  be the unit vector along the  $j$ th spoke edge. Then this is:

$$\sum_{j=1}^3 \sigma_j \mathbf{u}_j = \mathbf{0}. \quad (\text{B9})$$

We interpret this equation as the condition for the closure of the polygonal path with sides  $\sigma_j \mathbf{u}_j$ . Generally, when a vertex is in equilibrium, the forces acting on it can be seen as the sides of a closed *force polygon*. Note that in this force triangle the angles  $\alpha$  between the spoke edges become the ‘‘turning angles’’, so that e.g. the angle opposite side  $\sigma_1$  in the force triangle is  $\pi - \alpha_{2,3}$ . We can show that this triangle is closed using the (converse of the) law of sines, which amounts to proving that the following are all equal:

$$\sigma_1 / \sin \alpha_{2,3} = \sigma_2 / \sin \alpha_{3,1} = \sigma_3 / \sin \alpha_{1,2} \quad (\text{B10})$$

We will just show the first equality, as the proof of the others is exactly the same.

$$\frac{\sigma_1}{\sin \alpha_{2,3}} = \csc \alpha_{2,3} \left( \frac{\csc \alpha_{1,2}}{L_2} + \frac{\csc \alpha_{3,1}}{L_3} \right) \quad (\text{B11})$$

$$= \frac{\csc \alpha_{3,1} \csc \alpha_{2,3}}{L_3} + \frac{\csc \alpha_{3,1} \csc \alpha_{1,2}}{L_1} + \frac{-\csc \alpha_{3,1} (\cot \alpha_{2,3} + \cot \alpha_{1,2})}{L_2} \quad (\text{B12})$$

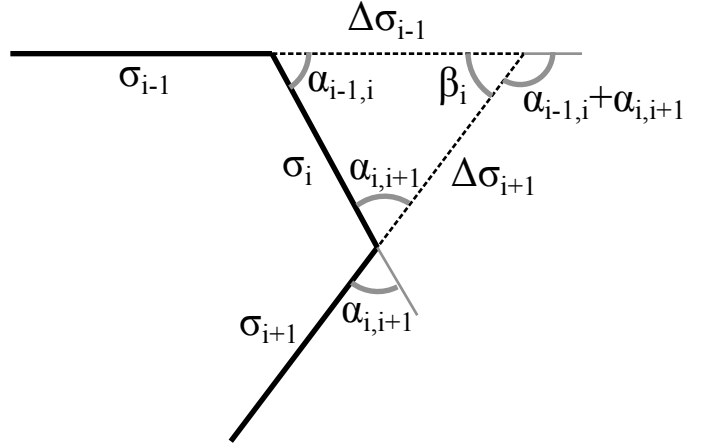


FIG. 12: Portion of the force polygon for the hub vertex considered during the induction. Force balance at the hub vertex is equivalent to the closure of the force polygon. Each edge in the figure is a vector parallel to the spoke edges whose length is equal to the magnitude of the stress component in that edge. Here we only show the forces along spokes  $i-1, i, i+1$  and how they change if spoke  $i$  were to be removed.

We will need the following trigonometric identity, equivalent to the sine addition rule:

$$\csc a \csc b = \csc(a + b)(\cot a + \cot b). \quad (\text{B13})$$

Note that  $-\csc \alpha_{3,1} = \csc(\alpha_{1,2} + \alpha_{2,3})$  since  $\alpha_{1,2} + \alpha_{2,3} + \alpha_{3,1} = 2\pi$ . Therefore by applying Eq. (B13) twice, we have,

$$\frac{\sigma_1}{\sin \alpha_{2,3}} = \frac{\csc \alpha_{3,1} \csc \alpha_{2,3}}{L_3} + \frac{-\csc \alpha_{2,3} (\cot \alpha_{1,2} + \cot \alpha_{2,3})}{L_1} \quad (\text{B14})$$

$$+ \frac{\csc \alpha_{2,3} \csc \alpha_{1,2}}{L_2} = \frac{\sigma_2}{\sin \alpha_{3,1}}. \quad (\text{B15})$$

For the induction step, assume that we have shown that we have force balance at the hub vertex in any wheel graph with  $n$  spokes with stresses given by Eq. (B2). Consider the star subgraph  $G_{n+1}$  of the wheel graph, consisting of  $n+1$  spoke vertices connected to the hub; we will reduce the force balance at its hub to force balance in the star graph  $G_{n,i}$  formed by removing (an arbitrary) spoke vertex  $i$  and the edge joining it to the hub. As in the argument for the base case, we will work with force polygons and prove that the closure of the force polygon  $P_{n,i}$  of  $G_{n,i}$  implies the closure of the force polygon  $P_{n+1}$  of  $G_{n+1}$ .

Note that the expression in Eq. (B2) for spoke  $j$  depends only on the lengths  $L_{j-1}, L_j, L_{j+1}$  and the angles  $\alpha_{j-1,j}$  and  $\alpha_{j,j+1}$ . This means that the self stress evaluated on corresponding spokes of  $G_{n+1}$  and  $G_{n,i}$  are identical except at the edges  $i-1, i, i+1$ . Thus  $P_{n,i}$  and  $P_{n+1}$  are identical except at those edges too. We will

prove that the situation is as depicted in Fig. 12. There, the edges of  $P_{n+1}$  are depicted as thick lines, with the dashed edges  $i-1, i+1$  of  $P_{n,i}$  overlaid.

To get started, we observe that the closure of  $P_{n,i}$  implies there is a vertex where the edges corresponding to spokes  $i-1$  and  $i+1$  (dashed in Fig. 12) intersect. We will denote lengths of edge  $i-1$  and  $i+1$  in  $P_{n,i}$  are  $\sigma_{i-1}^0$  and  $\sigma_{i+1}^0$ , respectively. In  $P_{n+1}$ , edges  $i-1$  and  $i+1$  can be taken to lie on the corresponding edges of  $P_{n,i}$  but they will in general have different lengths, which are simply  $\sigma_{i-1}$  and  $\sigma_{i+1}$ . For  $P_{n+1}$  to be closed, edge  $i$  must begin at the end point of  $i-1$  and end at the starting point of  $i+1$ . This means that there is a closed triangle with side lengths  $\Delta\sigma_{i-1} = \sigma_{i-1} - \sigma_{i-1}^0$ ,  $\Delta\sigma_{i+1} = \sigma_{i+1} - \sigma_{i+1}^0$ , and  $\sigma_i$  and whose angles are determined by the angles  $\alpha_{i-1,i}$  and  $\alpha_{i,i+1}$  between the spoke edges  $i-1, i$  and  $i+1$ . Note that the angle  $\beta_i = \pi - \alpha_{i-1,i} - \alpha_{i,i+1}$ .

To prove that this triangle is closed, we will again use the law of sines. For convenience, here are the formulas for the lengths:

$$\sigma_i = \frac{\csc \alpha_{i,i+1}}{L_{i+1}} + \frac{\csc \alpha_{i-1,i}}{L_{i-1}} \quad (B16)$$

$$\Delta\sigma_{i-1} = \frac{\csc \alpha_{i-1,i}}{L_i} + \frac{\csc \alpha_{i-2,i-1}}{L_{i-2}} \quad (B17)$$

$$\begin{aligned} & - \frac{\cot \alpha_{i,i+1} + \cot \alpha_{i-1,i}}{L_i} \\ & - \frac{\csc(\alpha_{i-1,i} + \alpha_{i,i+1}) - \csc \alpha_{i-2,i-1}}{L_{i+1}} \\ & + \frac{\cot(\alpha_{i-1,i} + \alpha_{i,i+1}) + \cot \alpha_{i-2,i-1}}{L_{i-1}} \end{aligned} \quad (B18)$$

$$\Delta\sigma_{i-1} = \frac{\csc \alpha_{i-1,i}}{L_i} - \frac{\csc(\alpha_{i-1,i} + \alpha_{i,i+1})}{L_{i+1}} \quad (B19)$$

$$\begin{aligned} & - \frac{\cot \alpha_{i-1,i} - \cot(\alpha_{i-1,i} + \alpha_{i,i+1})}{L_{i-1}} \\ & - \frac{\csc \alpha_{i,i+1}}{L_i} - \frac{\csc(\alpha_{i-1,i} + \alpha_{i,i+1})}{L_{i-1}} \\ & - \frac{\cot \alpha_{i,i+1} - \cot(\alpha_{i-1,i} + \alpha_{i,i+1})}{L_{i+1}}. \end{aligned} \quad (B19)$$

We will only show  $\sigma_i / \sin \beta_i = \Delta\sigma_{i-1} / \sin \alpha_{i,i+1}$ , as the

proof of the other identity is the same.

$$\frac{\sigma_i}{\sin \beta_i} = -\csc(\alpha_{i-1,i} + \alpha_{i,i+1}) \left( \frac{\csc \alpha_{i,i+1}}{L_{i+1}} + \frac{\csc \alpha_{i-1,i}}{L_{i-1}} \right) \quad (B20)$$

$$\begin{aligned} & - \frac{\cot \alpha_{i,i+1} + \cot \alpha_{i-1,i}}{L_i} \\ & = -\csc(\alpha_{i-1,i} + \alpha_{i,i+1}) \left( \frac{\csc \alpha_{i,i+1}}{L_{i+1}} + \frac{\csc \alpha_{i-1,i}}{L_{i-1}} \right) \quad (B21) \end{aligned}$$

$$\begin{aligned} & + \frac{\csc \alpha_{i,i+1} \csc \alpha_{i-1,i}}{L_i} \\ & = \csc \alpha_{i,i+1} \left( \frac{-\csc(\alpha_{i-1,i} + \alpha_{i,i+1})}{L_{i+1}} + \frac{\csc \alpha_{i-1,i}}{L_i} \right) \quad (B22) \end{aligned}$$

$$\begin{aligned} & - \frac{\csc \alpha_{i,i+1} (\cot \alpha_{i-1,i} - \cot(\alpha_{i-1,i} + \alpha_{i,i+1}))}{L_{i-1}} \\ & = \frac{\Delta\sigma_{i-1}}{\sin \alpha_{i,i+1}}. \quad (B23) \end{aligned}$$

where in the second and third equalities we have applied Eq. (B13). This completes the proof that Eqs. (B1) and (B2) define a self stress on the wheel graph.

### Appendix C: Vertex Quadratic Forms

Let us consider the quadratic form in Eq. (A6). This form has the interpretation as the energy if the wheel self stress is applied as a pre-stress [24]. Note that with our sign convention, this pre-stress places the spokes under compression and the outer edges under tension.

Using the same notation as in Section II, where  $h_0$  is the height of the vertex and  $h_1$  through  $h_N$  are the heights of the adjacent vertices, Eq. (A6) then reads

$$0 = \sum_{n=1}^N (g_{n,n+1} 2h_n h_{n+1} + f_n h_n^2 + A_n 2h_0 h_n) - h_0^2 \sum_{n=1}^N A_n, \quad (C1)$$

where

$$f_n = \frac{\cot \alpha_{n,n+1} + \cot \alpha_{n-1,n}}{L_n^2} \quad (C1)$$

$$g_{n,n+1} = -\frac{\csc \alpha_{n,n+1}}{L_n L_{n+1}} \quad (C2)$$

$$A_n = -f_n - g_{n,n+1} - g_{n-1,n} = \frac{\sigma_n}{L_n}. \quad (C3)$$

The corresponding matrix has three null directions, corresponding to the vertical translation and rotations about the  $x$ - and  $y$ -axes of the entire origami structure. We can remove these by setting  $h_0 = h_1 = h_N = 0$  explicitly. Then we have

$$0 = \sum_{n=2}^{N-1} (g_{n,n+1} 2h_n h_{n+1} + f_n h_n^2). \quad (C4)$$

This gives a tridiagonal matrix whose determinant,  $\chi(N)$ , can be computed to be

$$\chi(N) = \frac{\prod_{n=1}^{N-1} \csc \alpha_{n,n+1}}{\prod_{n=2}^{N-1} L_n^2} \sin \left( \sum_{n=1}^{N-1} \alpha_{n,n+1} \right). \quad (\text{C5})$$

This can be proven by induction using the continuant,

$$\chi(N+2) = f_{N+2} \chi(N+1) - g_{N+1, N+2}^2 \chi(N). \quad (\text{C6})$$

When all the angles between vertices are identical,  $\alpha_{n,n+1} \equiv \alpha$  and the lengths of the folds are also the same,  $L_n = L$ , the quadratic form of Eq. (C4) is also Toeplitz, and its eigenvalues can be determined explicitly by

$$\lambda_m = f + 2|g| \cos \left( \frac{m\pi}{N-1} \right) \quad (\text{C7})$$

for  $m$  ranging from 1 to  $N-1$ . For  $N$  folds,  $\alpha = 2\pi/N$ . Thus,

$$\lambda_m = 2 \frac{\csc(2\pi/N)}{L^2} \left[ \cos \left( \frac{2\pi}{N} \right) - \cos \left( \frac{m\pi}{N-1} \right) \right]. \quad (\text{C8})$$

Consequently,  $\lambda_1 < 0$  and the other eigenvalues are positive. Now consider changing the angles smoothly. Since no eigenvalue can change sign without the determinant  $\chi = 0$ , we see that Eq. (C5) implies that there is always one negative eigenvalue so long as the angles between any pair of adjacent folds remain between 0 and  $\pi$ . When  $N \geq 4$  there are thus eigenvalues of both signs, and there is always a solution to Eq. (C4) for a single vertex; the vertex is infinitesimally rigid when all eigenvalues have the same sign (as happens when  $N = 3$ , for instance).

We can get some physical intuition for the distribution of eigenvalues as follows. Under the wheel pre-stress corresponding to this quadratic energy, the negative eigenvector should correspond to an out-of-plane displacement that is maximally unstable. We can imagine that there is one that increases the lengths of the compressed spokes while not increasing the lengths of the outer edges too much, as such a motion will be destabilized by the stress. The other  $N-3$  motions correspond to out-of-plane displacements that are stabilized by the pre-stress, i.e. those that primarily increase the lengths of the outer edges.

The discussion above recovers a special case of a result of Kapovich and Millson [23] who studied the configuration space of origami vertices using techniques from the deformation theory of representations of  $SO(3)$ . In fact, they considered flat origami vertices that may fold back on themselves (allowing  $\alpha_{j,j+1} < 0$  for some  $j$ ) or have a different winding around the vertex ( $\sum_{j=1}^N \alpha_{j,j+1} = 2\pi w$ , for some integer  $w$  not necessarily equal to 1). The relevant result of their paper is the following

### Theorem 1 (Kapovich and Millson, 1997)

*Theorem 1.1(iii). Assume all planar angles satisfy  $0 < |\alpha_{j,j+1}| < \pi$ . The germ of the configuration space of an origami vertex with  $f$  forward-tracks,  $b$  back-tracks,*

*and winding  $w$  is isomorphic to the germ of the null-cone of a quadratic form with nullity 3, and signature  $(f-2w-1, b+2w-1)$ .*

Here  $f$  counts the number of forward-tracks, defined to be the planar angles with  $\alpha > 0$  and  $b$  counts the number of back-tracks, defined to be those angles with  $\alpha < 0$ .

We showed above the case of this theorem when  $f = N$ ,  $b = 0$  and  $w = 1$ , and in fact our sign convention for the sign of the quadratic form also agrees with theirs. (A change of sign swaps negative and positive eigenvalues, but of course leads to the same null-cone). Furthermore, it is easy to see that our observation that Eq. (C5) only vanishes when one of the  $\alpha$  is an integer multiple of  $\pi$  is consistent with their statement that the signature changes when any of  $f, b, w$  change. Indeed, Eq. (C4) for the quadratic form applies in full generality, and so we can actually use it to give a complete proof of Theorem 1.

**Proof of Theorem 1:** The first claim about the germ being isomorphic to the germ of the null-cone essentially states that the quadratic form we have derived in Eq. (C4) as the lowest order constraint on the configuration space does give an accurate picture of a neighborhood of the singular point (the flat state), i.e. that the second-order motions satisfying Eq. (C4) extend to true motions. For this we refer to Theorem 4 of [25] which gives an elementary proof of this fact. (In fact, [23] prove the stronger result that there is an analytic isomorphism between neighborhood germs.)

The rest of the theorem addresses the signature of the quadratic form. The nullity of 3 corresponds to the global isometries mentioned earlier. So we just need to derive the expression  $(f-2w-1, b+2w-1)$  for the number of (positive, negative) eigenvalues. Since the defining symmetric matrix is  $(n+1) \times (n+1)$  and  $f+b = n$  it is enough to show that the number of negative eigenvalues  $N_- = b+2w-1$ .

Suppose we have a real symmetric  $k \times k$  matrix  $M$ , and let  $\Delta_j$  is the determinant of the upper-left  $j \times j$  submatrix of  $M$  (the  $j$ th principal minor of  $M$ ). The key observation is that, provided none of the  $\Delta_j$  vanish,  $N_-$  is equal to the number of sign changes of the sequence  $\Delta_0 = 1, \Delta_1, \dots, \Delta_k$  [39].

Due to the tridiagonal nature of the stress matrix,  $\chi(j)$  is also an expression for  $\Delta_j$  of the stress matrix. So we just have to show that we get exactly  $b+2w-1$  sign changes. Let us consider the ratio:

$$\frac{\Delta_{j+1}}{\Delta_j} = \frac{\csc \alpha_{j-1,j}}{L_j^2} \frac{\sin \left( \sum_{n=1}^j \alpha_{n,n+1} \right)}{\sin \left( \sum_{n=1}^{j-1} \alpha_{n,n+1} \right)}. \quad (\text{C9})$$

This consists of two factors. The first factor  $\csc \alpha_{j-1,j}$  is negative if and only if  $\alpha_{j-1,j} < 0$ , i.e. when the  $j$ th planar angle is a back-track. The second factor is negative if and only if the two quantities  $\sum_{n=1}^{j-1} \alpha_{n,n+1}$  and  $\sum_{n=1}^j \alpha_{n,n+1}$  sandwich an integer multiple of  $\pi$ . Let us first assume

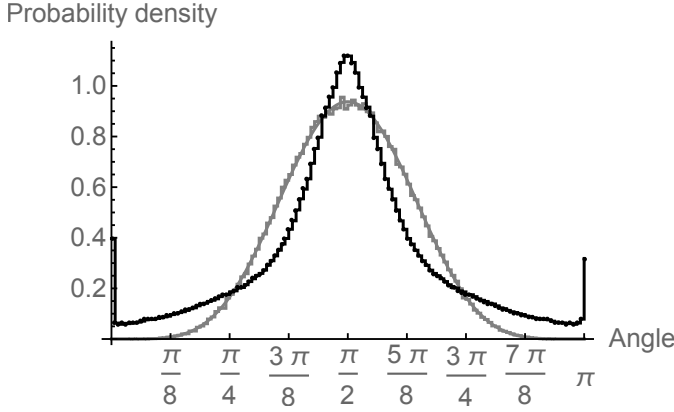


FIG. 13: The probability distribution for the angles between branch vectors in random origami with  $V_i = 6$  (black) compared to randomly distributed points on a 6-dimensional sphere (gray). The bin sizes are  $\pi/32$ . The solid gray line is an analytical prediction using Eq. 5 of Ref. [34].

that the second factor does not vanish (the first never will, by our assumptions on the  $\alpha$ 's).

We get a net negative sign in Eq. (C9) if and only if one of the following two possibilities occurs. Possibility A, the  $j$ th planar angle is a back-track and the partial sum  $\sum_{n=1}^j \alpha_{n,n+1}$  does not pass an integer multiple of  $\pi$ . If  $C_b$  is the number of back-track crossings over integer multiples of  $\pi$ , this occurs  $b - C_b$  times. Possibility B, the  $j$ th planar angle is a forward-track and the partial sum does cross an integer multiple of  $\pi$ . This occurs  $C_f$  times, where  $C_f$  is the number of forward-track crossings of integer multiples of  $\pi$ .

It follows that  $2w - 1$  is the *net* number of times  $C_f - C_b$  that integer multiples of  $\pi$  are crossed, since  $w$  is the total winding number. Therefore we have  $b - C_b + C_f = b + 2w - 1$  sign changes in total, as desired.

Finally, we treat the case where  $\Delta_j$  vanishes due to the partial sum  $\sum_{n=1}^j \alpha_{n,n+1}$  being equal to an integer multiple of  $\pi$ . However, as argued after Eq. (C8), we can perturb the angles  $\alpha$  to avoid these cases without changing the sign of the overall determinant (note that the angle sum in  $\chi(N)$  is equal to  $2\pi - \alpha_{N,1}$ ), and hence without changing the signature. Such a perturbation can also be chosen small enough so that  $f, b, w$  do not change, so the same formula applies.

This concludes the proof of Theorem 1.

#### Appendix D: High-dimensional geometry and random origami

To better understand how the branches of a random triangulated  $D = 1$  origami are distributed as directions in configuration space, we computed pair distribution functions between the branches, where the branches are interpreted as lines in the  $3V_i + 1$ -dimensional space of infinitesimal changes in dihedral angle. (Note that the

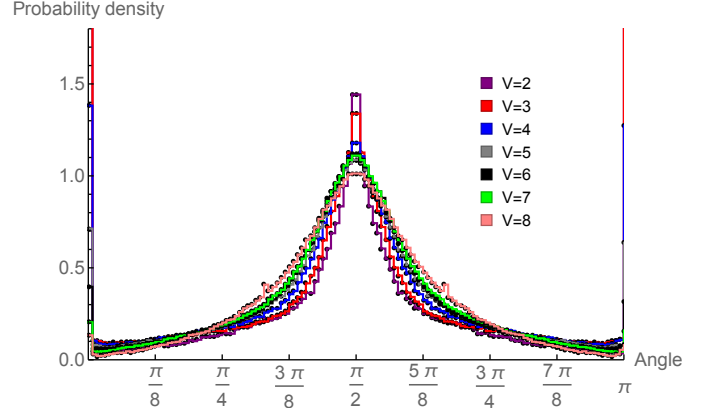


FIG. 14: (color) The probability distribution that any two pairs of branches will be a given angle part for random origami with  $V = 2 - 8$  vertices. The bin sizes are  $\pi/32$ .

branches lie in a  $V_i + 1$ -dimensional linear subspace, as not all sets of dihedral angles are induced by height displacements). Computationally, given a particular configuration, we take the numerically computed branches given as vectors of vertex heights and transform them into vectors of dihedral angles. Here we choose to work with both  $\pm$  ends of the branch line, so that we have  $2^{V_i+1}$  vectors. We then compute the  $(2^{V_i+1})^2$  angles coming from dot products between all ordered pairs of branches. These angles are the distances between branches as points on the  $V_i$ -dimensional sphere. For each  $V_i$  we compute these angles for all of the configurations in Table I to create histograms of the angles, or pair distribution functions.

In Fig. 13, we show the histogram of the angle between pairs of branches for  $V = 6$  using bins of size  $\pi/128$  (black line). We compare the results to random points on a  $V_i$ -dimensional sphere (gray line). The data shows that random origami has a slight enhancement in the number of orthogonal branches but a more prominent enhancement at the two tails of the distribution. In particular, the results of Ref. [34] imply that for random points on a sphere, the angle distribution approaches a Gaussian with variance going to zero. However, the tails of the distributions of angles between branches in random origami appear to decay exponentially, rather than as a Gaussian.

To indicate what happens as  $V_i$  changes, Fig. 14 depicts the distributions for random origami with vertices from  $V_i = 2 - 8$ , again binning the results into bins of size  $\pi/128$ . Since the branches have no natural orientation, for each angle  $\theta$ , we also include the angle  $\pi - \theta$ ; as a consequence, for small  $V_i$ , there is an enhancement for branches that are almost  $\pi$  apart in angle, since each branch has an angle 0 and  $\pi$  with itself. It is interesting to note that while the distributions for  $V_i = 6, 7$  very nearly coincide, they differ significantly from that of  $V_i = 8$ . We do not believe that this is due to a lack of data. Even though we computed fewer configurations at  $V_i = 8$ , each configuration has twice the number of branches and hence

four times as many angle pairs, so the number of data

points going into the histograms is comparable.

---

[1] J. L. Silverberg, J.-H. Na, A. A. Evans, B. Liu, T. C. Hull, C. D. Santangelo, R. J. Lang, R. C. Hayward, and I. Cohen, *Nature materials* **14**, 389 (2015).

[2] S. Waitukaitis, R. Menaut, B. G. Chen, and M. van Hecke, *Phys. Rev. Lett.* **114**, 055503 (2015).

[3] J.-H. Na, A. A. Evans, J. Bae, M. C. Chiappelli, C. D. Santangelo, R. J. Lang, T. C. Hull, and R. C. Hayward, *Advanced Materials* **27**, 79 (2015).

[4] D. Sussman, Y. Cho, T. Castle, X. Gong, E. Jung, S. Yang, and R. Kamien, *Proc. Natl. Acad. Sci.* **112**, 7449 (2015).

[5] J. Ryu, M. D’Amato, X. Cui, K. N. Long, H. J. Qi, and M. L. Dunn, *Applied Physics Letters* **100**, 161908 (2012).

[6] M. T. Tolley, S. M. Felton, S. Miyashita, D. Aukes, D. Rus, and R. J. Wood, *Smart Materials and Structures* **23**, 094006 (2014).

[7] Y. Liu, M. Miskiewicz, M. J. Escutie, J. Genzer, and M. D. Dickey, *Journal of Applied Physics* **115**, 204911 (2014).

[8] T. Tachi and T. C. Hull, in *ASME 2016 International Design Engineering Technical Conferences and Computers and Information in Engineering Conference* (American Society of Mechanical Engineers, 2016), pp. V05BT07A029–V05BT07A029.

[9] Z. Y. Wei, Z. V. Guo, L. Dudte, H. Y. Liang, and L. Mahadevan, *Phys. Rev. Lett.* **110**, 215501 (2013).

[10] J. L. Silverberg, A. A. Evans, L. McLeod, R. C. Hayward, T. Hull, C. D. Santangelo, and I. Cohen, *Science* **345**, 647 (2014).

[11] T. Tachi, in *Proceedings of the Tenth International Association for Shell and Spatial Structures (IASS) Symposium* (2010), pp. 771–782.

[12] A. Evans, J. Silverberg, and C. Santangelo, *Phys. Rev. E* **92**, 013205 (2015).

[13] C. Lv, D. Krishnaraju, G. Konjevod, H. Yu, and H. Jiang, *Scientific reports* **4**, 5979 (2014).

[14] M. Schenk and S. D. Guest, *Proceedings of the National Academy of Sciences* **110**, 3276 (2013).

[15] K. Miura, *Proc. 31st Congr. Int. Astronaut. Federation IAF-8 0-A* **31**, 1 (1980).

[16] S. Pellegrino, *Deployable Structures* (Springer-Verlag Wien, 2001).

[17] T. Hull, in *Third International Meeting of Origami Science* (2002), pp. 29–38.

[18] B. Ballinger, M. Damian, D. Eppstein, R. Flatland, J. Ginepro, and T. Hull, in *Proceedings of the Twenty-Sixth Annual ACM-SIAM Symposium on Discrete Algorithms* (Society for Industrial and Applied Mathematics, 2015), pp. 136–147.

[19] Z. Abel, J. Cantarella, E. D. Demaine, D. Eppstein, T. C. Hull, J. S. Ku, R. J. Lang, and T. Tachi, *Journal of Computational Geometry* **7**, 171 (2016).

[20] V. Brunck, F. Lechenault, A. Reid, and M. Adda-Bedia, *Phys. Rev. E* **93**, 033005 (2016).

[21] B. G. Chen, B. Liu, A. A. Evans, J. Paulose, I. Cohen, V. Vitelli, and C. Santangelo, *Physical review letters* **116**, 135501 (2016).

[22] C. D. Santangelo, *Annual Review of Condensed Matter Physics* (2017).

[23] M. Kapovich and J. J. Millson, *Publ. RIMS, Kyoto Univ.* **33**, 1 (1997).

[24] R. Connelly and W. Whiteley, *SIAM J. Discrete Math.* **9**, 453 (1996).

[25] E. D. Demaine, M. L. Demaine, D. A. Huffman, T. C. Hull, D. Koschitz, and T. Tachi, in *Proceedings of the International Association for Shell and Spatial Structures (IASS) Symposium* (2016), pp. 1–10.

[26] I. Streinu and W. Whiteley, *Single-Vertex Origami and Spherical Expansive Motions* (Springer Berlin Heidelberg, Berlin, Heidelberg, 2005), pp. 161–173, ISBN 978-3-540-32089-0, URL [http://dx.doi.org/10.1007/11589440\\_17](http://dx.doi.org/10.1007/11589440_17).

[27] R. Connelly, *Adv. in Math.* **37**, 272 (1980).

[28] A. Morgan and A. Sommese, *Applied Mathematics and Computation* **24**, 115 (1987).

[29] T. Hull, private communication.

[30] J. Graver, B. Servatius, and H. Servatius, *Combinatorial Rigidity* (American Mathematical Society, 1993), ISBN 9780821838013.

[31] T.-S. Tay and W. Whiteley, *Structural Topology* **11**, 21 (1985).

[32] A. Nixon and E. Ross, arXiv preprint (2012), 1203.6623.

[33] C. Borcea and I. Streinu, *Discrete & Computational Geometry* **31**, 287 (2004), ISSN 1432-0444, URL <http://dx.doi.org/10.1007/s00454-003-2902-0>.

[34] T. Cai, J. Fan, and T. Jiang, *Journal of Machine Learning Research* **14**, 1837 (2013).

[35] M. Stern, M. Pinson, and A. Murugan, arXiv preprint (2017), 1703.04161.

[36] J. Capco, M. Gallet, G. Grasegger, C. Koutschan, N. Lubbes, and J. Schicho, arXiv preprint (2017), 1701.05500.

[37] M. C. Holmes-Cerfon, *SIAM Review* **58**, 229 (2016), <https://doi.org/10.1137/140982337>, URL <https://doi.org/10.1137/140982337>.

[38] Wikipedia, *Crossed ladders problem — Wikipedia, the free encyclopedia* (2016), [Online; accessed 27-March-2017], URL [https://en.wikipedia.org/w/index.php?title=Crossed\\_ladders\\_problem&oldid=750505743](https://en.wikipedia.org/w/index.php?title=Crossed_ladders_problem&oldid=750505743).

[39] E. Ghys and A. Ranicki, in *Six papers on signatures, braids and Seifert surfaces* (Soc. Brasil. Mat., Rio de Janeiro, 2016), vol. 30 of *Ensaios Mat.*, pp. 1–173.